Super-Resolution Doppler Velocity Estimation by Kernel-Based Range–τ Point Conversions for UWB Short-Range Radars

Masafumi Setsu, Takumi Hayashi, Jianghaomiao He, and Shouhei Kidera, *Member, IEEE*

***Abstract*— Lower band ultrawideband (UWB) Doppler radar is promising for through-wall imaging, e.g., human body detection in rescue scenarios. The inherent problem with pulse-Doppler radar is the tradeoff between the Doppler velocity resolution and the resulting temporal resolution that makes it difficult to conduct real-time target tracking, because the separation of micro-Doppler velocities of the human body requires a higher Doppler velocity resolution. This problem is particularly severe for lower band UWB radar systems, which are required to attain a sufficient penetration depth in concrete material in the through-the-wall imaging scenario. Because UWB signals generally have large fractional bandwidths, the reflected pulse is located over a range gate along the slow-time direction; this is well known as the range walk problem. As a promising solution to this problem, this article newly introduces a technique for a super-resolution Doppler velocity estimation algorithm based on Gaussian kernel density estimation, which converts observed range–τ points to Doppler-associated ranges. In addition, this approach makes an important contribution for super-resolution range extraction with a compressed sensing (CS) filter, which is combined with the range-point migration (RPM) method for human body imaging associated with micro-Doppler components. 2-D or 3-D numerical simulations, including human body imaging scenario, demonstrate that the proposed method allows both accurate Doppler velocity estimation and human body imaging, which can be updated at the pulse-repetition interval.**

***Index Terms*— Compressed sensing (CS), kernel density estimation, micro-Doppler for human body, pulse Doppler radar, range-point migration (RPM), through-the-wall imaging (TWI), ultrawideband (UWB) radar.**

I. Introduction

ULTRAWIDEBAND (UWB) microwave radar can be used to attain both a high range resolution and deep penetration in low-loss materials, such as concrete materials and soil. UWB short-range radar is thus a promising tool for through-the-wall imaging (TWI), detecting human bodies buried under collapsed structures at disaster sites, and identifying hostages and terrorists in security operations. To discriminate human bodies from surrounding objects, it is promising that one exploits the micro-Doppler component generated by different motions of human parts, such as arms, legs, and the head, and a pulse-Doppler radar system is thus promising for the above applications. In the case of high-frequency radar systems, such as a millimeter-wave radar system, Fourier-transform-based Doppler processing could provide a sufficiently higher Doppler velocity resolution [1], [2]. In the TWI-UWB radar model, however, the center frequency of the pulse should be lower than that of a millimeter wave for the pulse to accomplish deeper penetration in concrete materials, resulting in a lower Doppler velocity resolution. This negative effect necessitates a longer coherent integration time (on the order of 100 ms) to maintain a sufficient Doppler velocity resolution (on the order of 0.1 m/s). In addition, the fractional bandwidth of a UWB signal usually exceeds more than 20%, and the pulses received from the first and last pulse hits cannot overlap because the target may move during long observation, thus worsening the effective Doppler velocity resolution. This problem is recognized as the range walk (RW) effect [3].

Many studies have been conducted to address the RW effect by applying the Hough transform [4]–[6], the keystone transform [7], [8], or a motion-tracking approach [9]. In particular, the Radon Fourier transform (RFT) method was first proposed in [10], and extensions have subsequently been developed, such as the Radon fractional Fourier transform (RFRFT) in [11] and Radon-Lv's distribution (RLVD) in [12]. However, because these methods assume a high-speed target, such as an aircraft or missile, they do not require such a long integration time with lower Doppler velocity resolution (on the order of 10 m/s) and need not consider Doppler velocity variations in the coherent integration times. In addition, they basically require target tracking and motion compensation to process the data in order to obtain a long coherent integration time. As other approaches, a method of target tracking and Doppler estimation based on texture analysis has been proposed to achieve supertemporal-resolution Doppler velocity estimation [17]. In this approach, the instantaneous Doppler velocity is calculated from the texture angle, which is defined as the ratio of the partial derivatives of the signal strengths along the first and slow directions. However, this approach requires a pixel connection procedure for the texture angles to deal with interference, which becomes extremely complicated and computationally

Manuscript received April 25, 2019; revised September 23, 2019; accepted October 20, 2019. This work was supported by the Japan Science Technology Agency, Precursory Research for Embryonic Science and Technology (PRESTO), under Grant JPMJPR1771. *(Corresponding author: Shouhei Kidera.)*

M. Setsu, T. Hayashi, and J. He are with the Graduate School of Informatics and Engineering, University of Electro-Communications, Tokyo 1828585, Japan.

S. Kidera is with the Graduate School of Informatics and Engineering, University of Electro-Communications, Tokyo 1828585, Japan, and also with the Japan Science Technology Agency, PRESTO, Saitama 3320012, Japan (e-mail: kidera@uec.ac.jp).

Color versions of one or more of the figures in this article are available online at http://ieeexplore.ieee.org.

Digital Object Identifier 10.1109/TGRS.2019.2949104

expensive when more targets are introduced. Furthermore, due to the partial derivative operation, this technique is generally sensitive to small fluctuations in the signal strength. As other approaches overcome the limit of the Doppler frequency resolution, higher resolution time–frequency analyses have been developed, such as the Wigner–Ville distribution (WVD) [13], the Fourier–Bessel transform (FBT) [14], or the pseudo Wigner distribution (SPWD) [15], [16]. Although those methods overcome the limitation of the Doppler velocity resolution of the short-time Fourier transform (STFT)-based methods, they also require the assumption that the envelope of received pulses should be overlapped along the slow-time direction to apply the coherent integration, and then do not directly address the RW problem assumed in this article.

To overcome the above difficulty, this article newly introduces Gaussian kernel-based Doppler velocity estimation based on range–τ points' conversion, which we recently proposed [18]. The first step of the proposed algorithm involves range–τ points being extracted from the local maxima of fast- and slow-time (denoting τ) maps of the received signal strengths. Each inclination of a range–τ point (i.e., the instantaneous Doppler velocity) is then accurately determined by considering the distribution of the neighboring range–τ points using a statistical approach with the Gaussian kernel density estimator. The proposed Doppler velocity estimation method was inspired by the range-point migration (RPM) algorithm, which does not require the connection of so-called range points [19]. The proposed method has a similar feature in that it avoids the need for a process for connecting or tracking neighboring range–τ points, which realizes a significant advantage over conventional motion-tracking approaches. In addition, the proposed method has a significant advantage over the traditional coherent integration approaches that a Doppler velocity at each slow time (each range–τ point) can be determined without a lower limitation of velocity resolution, that is, our proposed method simultaneously achieves both higher temporal resolution [being identical to the pulse repetition interval (PRI)] and accurate Doppler velocity estimation, even in the RW scenario.

Furthermore, this article introduces a specific example of human imaging scenario, where the micro-Doppler velocity is associated with each range point with higher accuracy and temporal resolution, and is exploited as data clustering in the Doppler-associated RPM method [2], reducing the calculation time and enhancing imaging accuracy. Additionally, to obtain a higher range resolution with narrower band UWB radar, compressed sensing (CS)-based range extraction, namely, the range profile estimation scheme [20], is introduced to the present algorithm. A large number of impulsive responses from the CS-based filter make the RW effect more serious in traditional approaches due to considerably larger fractional bandwidth; however, the proposed Doppler velocity estimation completely addresses the above issue and maximizes the benefit of the CS filter when applied to imaging. The results of numerical simulations of a TWI application conducted employing the 2-D finite-difference time-domain (FDTD) method demonstrate that the proposed method remarkably enhances both the Doppler velocity resolution and the temporal resolution, even for multiple target models. Finally, the 3-D numerical analysis, considering human mimicking objects (an aggregation of ellipsoids), demonstrates that the proposed method offers a more accurate human body image and motion with higher temporal resolution.

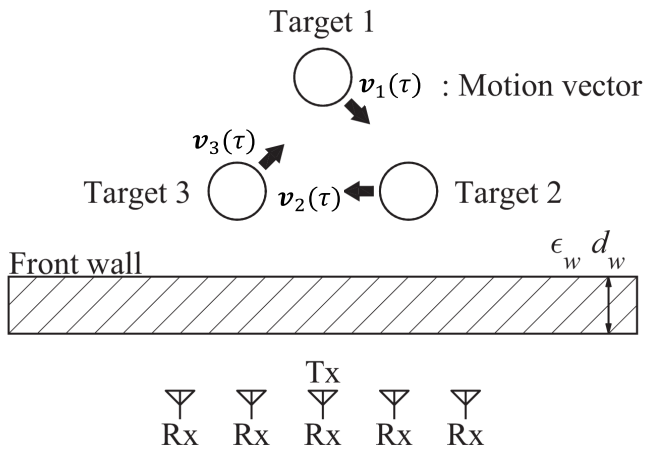

Fig. 1. Observation model.

The observation model presented in Sections II and III describes the principle and methodology of the proposed Doppler velocity method based on Gaussian kernel estimation. In Section IV, the 2-D FDTD numerical analysis and experimental validations are presented as a means of rotating multiple spherical targets and are compared with the traditional Fourier transform-based method. Section V introduces the incorporation algorithm with a CS-based range extraction filter and the RPM-based 3-D imaging method, assuming a 3-D human body imaging scenario. The conclusion and some additional discussion are presented in Section VI.

II. Observation Model and Range–τ Point Extraction

Fig. 1 shows the observation model of the TWI scenario. Multiple targets with arbitrary shapes and motions are assumed, while their locations, shapes, and velocities are not given. The kth target has a motion vector $\boldsymbol{v}_k(\tau)$, which is a variable with respect to the slow time τ, where it is sampled by the PRI. Omnidirectional antennas are arranged as a single transmitter and multiple receivers. The transmitting and receiving antennas are, respectively, located at $\boldsymbol{L}_{\mathrm{T}} = (X_{\mathrm{T}}, 0)$ and $\boldsymbol{L}_{\mathrm{R}} = (X_{\mathrm{R}}, 0)$. A number of pulses are transmitted from the transmitting antenna with the fixed PRI, and are received at the multiple receiving antennas. A concrete wall with thickness d_w is simulated in front of the array with relative permittivity, ε_w, and conductivity, σ_w, which are regarded as the given parameters in any method. For each combination of $\boldsymbol{L}_{\mathrm{T}}$ and $\boldsymbol{L}_{\mathrm{R}}$, the output of a filter (e.g., a matched, Wiener, or CS filters) of the recorded range–τ signal is denoted $s(\boldsymbol{L}_{\mathrm{T}}, \boldsymbol{L}_{\mathrm{R}}, R', \tau')$, where τ' is the slow-time sampled at the PRI. $R' = ct/2$ denotes the measured range, where c is the speed of radio wave in air and t is the fast time. The range–τ point

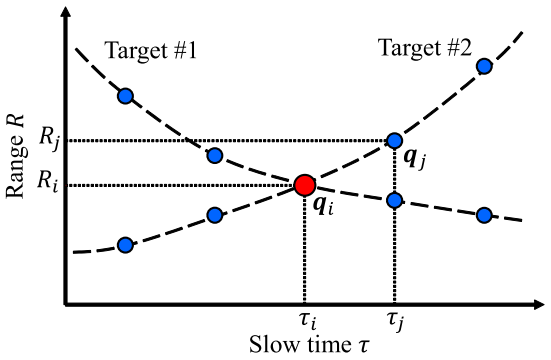

Fig. 2. Relationship among the focused range–τ point (red solid circle) $\boldsymbol{q}_i$ and the others (blue solid circles) in the range–τ space.

$\boldsymbol{q} \equiv (\boldsymbol{L}_\mathrm{T}, \boldsymbol{L}_\mathrm{R}, R, \tau)$ is then extracted from the set of local maxima of $s(\boldsymbol{L}_\mathrm{T}, \boldsymbol{L}_\mathrm{R}, R', \tau')$ as follows:

$$\left.\begin{aligned} &\frac{\partial s(\boldsymbol{L}_\mathrm{T}, \boldsymbol{L}_\mathrm{R}, R', \tau')}{\partial \tau'} = 0 \\ &s(\boldsymbol{L}_\mathrm{T}, \boldsymbol{L}_\mathrm{R}, R', \tau') \geq \alpha \max_{R', \tau'} s(\boldsymbol{L}_\mathrm{T}, \boldsymbol{L}_\mathrm{R}, R', \tau') \end{aligned}\right\} \quad (1)$$

where α denotes the threshold parameter. If the Nyquist criteria are satisfied for the fast-time direction, the measured range R can be accurately determined beyond the range resolution by introducing an over-sampling scheme, such as Sinc function-based interpolation.

III. Proposed Doppler Velocity Estimation Method

A. Kernel-Based Doppler Velocity Estimation Algorithm

To overcome the lower limitation of the Doppler velocity estimation in the Fourier-transform-based analysis, a novel algorithm suited to signals with lower center frequencies and larger fractional bandwidth pulses that are often encountered in UWB-TWI applications is proposed for Doppler velocity extraction. Fig. 2 depicts the relationship between the focused range–τ point $\boldsymbol{q}_i$ and others in the range–τ space. The inclination between the focused range–τ point as $\boldsymbol{q}_i$ and the neighboring range–τ points as $\boldsymbol{q}_j$ provides us the estimation of the Doppler velocity on $\boldsymbol{q}_i$. Thus, the proposed method tries to convert each $\boldsymbol{q}_i$ to the associated Doppler velocity by using the group of neighboring range–τ points. However, if a sensor receives multiple responses from multiple targets, it becomes extremely difficult to identify the connections between specific range–τ points; this problem is analogous to the joint problem of the DOA and range in spatial interferometry, which has been solved using the existing RPM algorithm [19]. Therefore, by introducing the RPM-based conversion scheme, the optimal Doppler velocity can also be determined by avoiding the connecting or tracking process. The proposed method also uses Gaussian kernel density estimation to calculate a probability function for the Doppler velocity, using the number of Doppler velocity samples defined as every possible combination of range–τ points. According to the above principle, the proposed method determines the optimal Doppler velocity $\hat{v}_d(\boldsymbol{q}_i)$ for $\boldsymbol{q}_i$ as

$$\hat{v}_d(\boldsymbol{q}_i) = \arg\max_{v_d} \sum_j \exp\left(-\frac{|s(\boldsymbol{q}_i) - s(\boldsymbol{q}_j)|^2}{2\sigma_s^2}\right) \times \exp\left(-\frac{|\tau_i - \tau_j|^2}{2\sigma_\tau^2}\right) \exp\left(-\frac{|v_d - v_{d,i,j}|^2}{2\sigma_{v_d}^2}\right) \quad (2)$$

where s is the signal strength of range–τ point $\boldsymbol{q}$, and σ_s, σ_τ, and σ_{v_d} are constants, which are determined empirically, but considering the S/N, PRI, and average Doppler velocity variations. In particular, if σ_τ becomes much larger than the PRI, an accurate Doppler velocity estimation would not be possible, given that the temporal variation of the Doppler velocity is not negligible in the order of PRI, and therefore should be set as a couple of PRI. $v_{d,i,j}$ is defined as $v_{d,i,j} \equiv (R_j - R_i)/(\tau_j - \tau_i)$. The term $\exp(-(|v_d - v_{d,i,j}|^2)/2\sigma_{v_d}^2)$ denotes the Gaussian kernel probability function for the sampled $v_{d,i,j}$. The rationale for introducing the weight function of $\exp(-((|\tau_i - \tau_j|^2)/2\sigma_\tau^2))$ is that the Doppler velocity could change over the PRI, such that the Doppler velocity calculated by the neighboring range–τ points of $\boldsymbol{q}_i$ should be more reliable for accurately estimating the Doppler velocity $\hat{v}_{d,i}$. In addition, the weight function $\exp((-(|s(\boldsymbol{q}_i)) - s(\boldsymbol{q}_j)|^2/2\sigma_s^2))$ is based on the signal strength for the range–τ points caused by the same target being almost the same level. Note that, (2) assesses the degree of accumulation of each converted Doppler velocity, which is calculated from all possible combinations of range–τ points considering the slow-time separation, and the signal strength difference as a weighting function. While the differential operation (using only the neighboring range–τ points) is quite sensitive to range errors caused by noise, the proposed method would be noise-robust if the results were to be averaged by the number of range–τ points with the above weighting factor.

Note that the proposed method focuses on numerous inclinations [Doppler velocities, denoted as $v_{d,i,j}$ in (2)] and on each range–τ point ($\boldsymbol{q}_i$), as determined by all possible combinations of range–τ points [$\boldsymbol{q}_j$, $(i \neq j)$], not only neighboring range–τ points. This could enhance the robustness of the range errors in those cases with rich interference. In addition, this method has unique advantages in that there is no lower limit of the Doppler velocity resolution, in principle, when focusing on the inclination extraction for discrete range–τ points and that the method overcomes the tradeoff between the Doppler velocity resolution and temporal resolution in the Fourier transform-based analysis, i.e., an instantaneous Doppler velocity is available using the proposed method. In addition, the Doppler velocity optimization defined in (2) does not require the connecting or tracking of range–τ points, greatly reducing the computational cost and avoiding the dependence that occurs in connecting the results, which is an advantage taken from the method presented in [17]. Furthermore, even in situations with high levels of interference in the range–τ space, the accuracy of the Doppler velocity estimation is guaranteed if well-resolved range–τ responses are available.

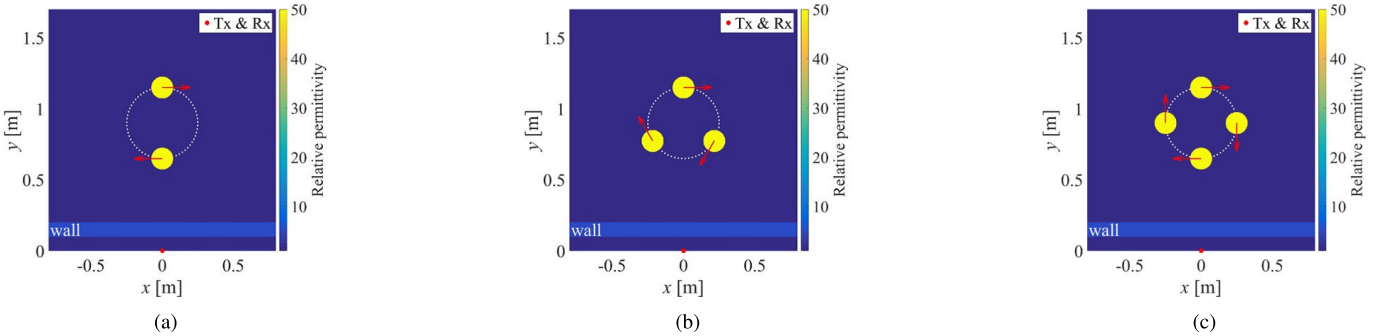

Fig. 3. Initial dielectric maps in each case. Red solid circle: transmitting and receiving antennas' location. (a) Case 1 (two targets). (b) Case 2 (three targets). (c) Case 3 (four targets).

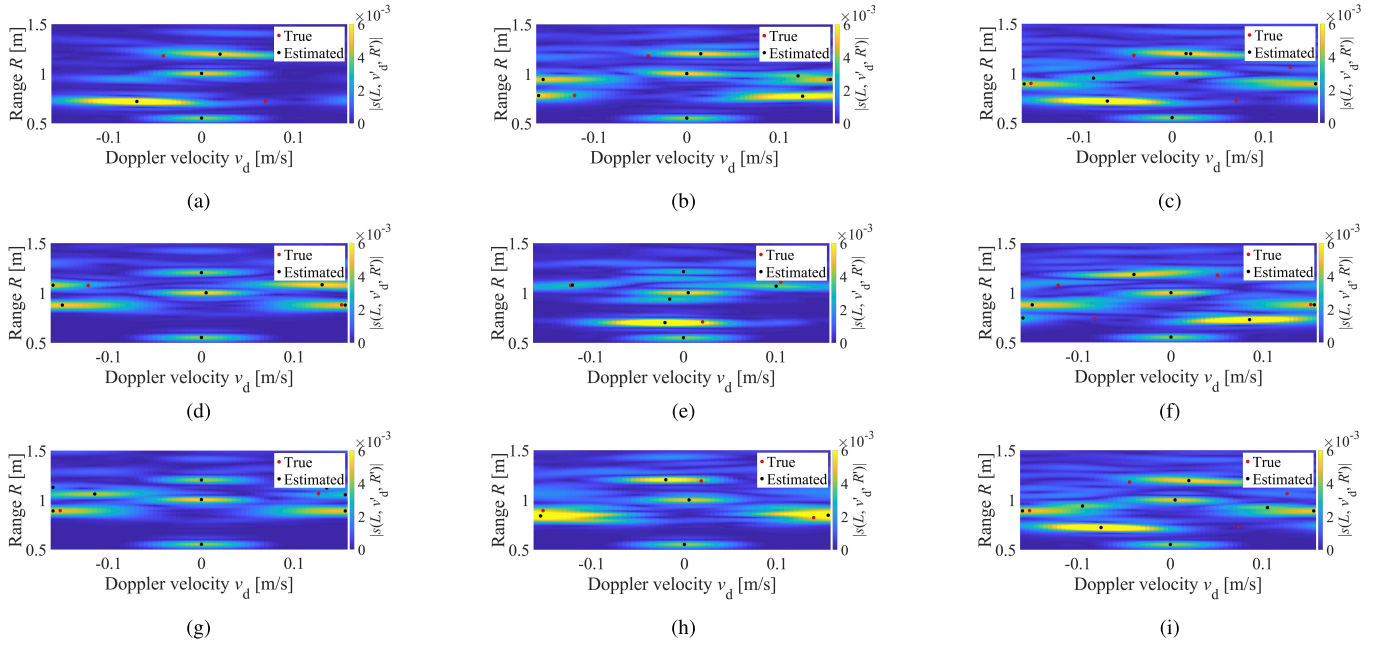

Fig. 4. Range-Doppler velocity responses by the STFT-based analysis of each temporal window with the width of 1.25 s. (a), (d), and (g) Case 1 (two targets). (b), (e), and (h) Case 2 (three targets). (c), (f), and (i) Case 3 (four targets). Red solid circles: actual Doppler velocities. Black solid circles: estimated Doppler velocities from local maxima of responses.

IV. Performance Evaluation for Doppler Velocity Estimation

A. Numerical Simulation Test

1) Numerical Setting: This section specifies the evaluation for Doppler velocity estimation of the method proposed in Section III-A, using the 2-D FDTD numerical simulation, assuming the TWI situation. The transmitting signal forms a Gaussian-modulated sinusoidal pulse, where the center frequency is 3.0 GHz corresponding to the center wavelength of $\lambda = 100$ mm, and the effective bandwidth is 2.0 GHz. A single set of transmitting and receiving antennas is located on the origin. A rectangular wall is located in front of the antenna with thickness $d_w = 1.0\lambda$, relative permittivity $\varepsilon_w = 5.0$, and conductivity $\sigma_w = 0.005$ S/m. A number of circle-shaped objects (mimicking a human), with relative permittivity of 50 (assuming a nondispersive and homogeneous material) and conductivity of 1.0 S/m, travel along a circular orbit with an origin at $(0.0\lambda, 9.0\lambda)$ and a radius of 2.5λ. All objects have the same velocity of 0.5π m/s and are equally spaced. The total observation time is set at $T_c = 1.0$ s, where the number of pulse hits is 64. The zero-Doppler components are suppressed by removing the average component of $s(\boldsymbol{L}, \tau', R')$ along the τ direction. Here, we test the cases of different numbers of targets. Fig. 3 shows the initial dielectric property map in each case.

2) Noiseless Scenario: Here, we consider the case that noise is absent to estimate the systematic error of the proposed method. Fig. 4 shows the results of the STFT-based Doppler-range maps for each case, where the temporal window is slided along the slow-time direction with the width of 1.25 s, denoting the nominal Doppler velocity resolution as 0.04 m/s. These results show that the STFT-based Doppler analysis suffers from inaccuracy and lower resolution for the Doppler velocity estimation, because the shorter integration time in the STFT results in lower Doppler velocity resolution, which is the inherent limitation of Fourier transform-based analysis. It is noted that a larger fractional bandwidth signal (e.g., UWB pulse) further degrades the Doppler velocity resolution, because the slow-time interval

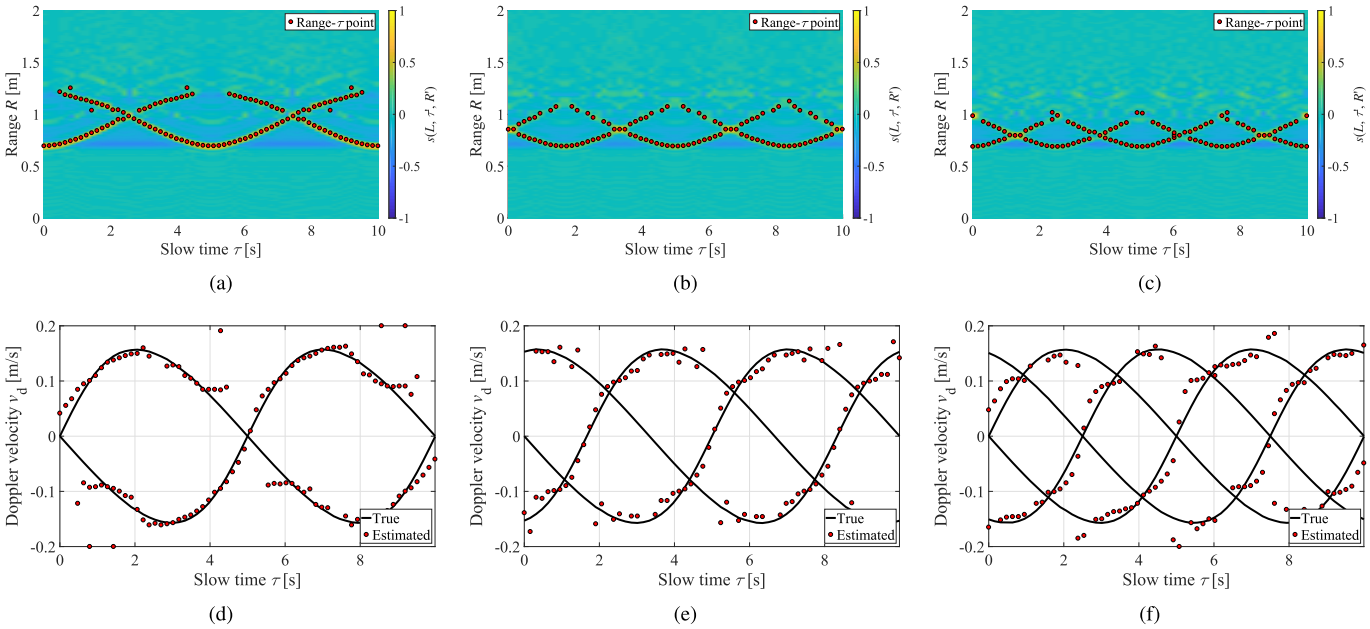

Fig. 5. (a)–(c) Responses of filter and extracted range–τ points in cases 1–3, respectively. (d)–(f) Estimated Doppler velocities (red solid circles) by the proposed method at cases 1–3, respectively.

of pulse overlapping becomes smaller than that for a signal having smaller fractional bandwidth. Fig. 5(a)–(c) presents the distributions of the strength of responses of filter along the slow-time direction and the extracted range–τ points. These figures show that the envelopes of the reflection responses do not largely overlap along the slow-time direction. That is, the RW effect is never negligible. These plots show that the Doppler velocity of each target considerably varies along the slow-time direction due to rotating motion and the long observation time, resulting in a lower and inaccurate Doppler velocity estimation based on STFT analysis. In contrast, Fig. 5(d)–(f) shows the estimated Doppler velocities for each slow-time snapshot by the proposed kernel-based Doppler analysis described in Section III-A at each case. Here, $\sigma_s = 0.7$, $\sigma_{v_d} = 0.04$ m/s, and $\sigma_\tau = 634$ ms are set in (2). Note that interference at the same range gate results in inaccurate Doppler velocity estimation as shown in the plots. In addition, some Doppler velocities are missed in the estimation, especially in Fig. 5(e) and (f), because an object enters an area of shadow projected by other objects. In most snapshots, however, the proposed method accurately estimates the Doppler velocity beyond the nominal Doppler frequency resolution at each slow time, i.e., the higher temporal resolution and Doppler frequency resolution are simultaneously available. The required processing time of the proposed Doppler velocity estimation is within 0.3 s in any case when using an Intel Xeon CPU E5-1620 v2 (3.7 GHz) processor with 16-GB RAM, showing that the proposed method has an advantage in terms of the calculation cost over methods requiring connecting or tracking processes in [9] and [17].

For quantitative evaluation, the error of the Doppler velocity estimation is defined as

$$e_{v_d}\left(v_{d,i}^{\mathrm{est}}\right) \equiv \min_{v_d^{\mathrm{true}}} \left|v_{d,i}^{\mathrm{est}} - v_d^{\mathrm{true}}\right|, \quad (i = 1, 2, \ldots, N_{\mathrm{T}}) \qquad (3)$$

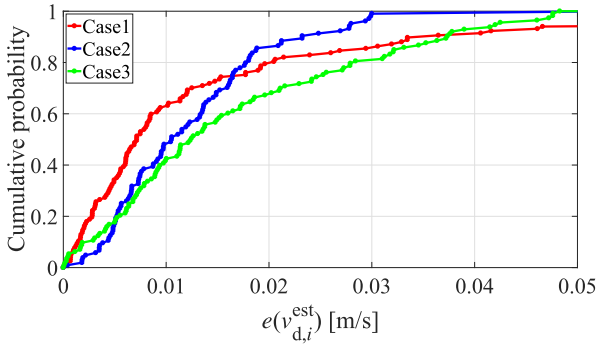

Fig. 6. Cumulative probability distribution of the errors for the Doppler velocity estimation in each case.

where $v_{d,i}^{\mathrm{est}}$ is the estimated Doppler velocity of the ith range–τ point $\boldsymbol{q}_i$, v_d^{true} denotes the true Doppler velocities at each slow-time snapshot, and N_{T} is the total number of $v_{d,i}^{\mathrm{est}}$. Fig. 6 shows the cumulative distribution of $e_{v_d}(v_{d,i}^{\mathrm{est}})$ for each case. The cumulative probabilities satisfying $e_{v_d}(v_{d,i}^{\mathrm{est}}) < 0.02$ m/s is 79.5% for case 1, 84.6% for case 2, and 67.3% for case 3, where the nominal Doppler velocity resolution in Fig. 4 is 0.04 m/s. This quantitative evaluation shows that our proposed method accurately estimates the Doppler velocities of multiple targets even in using lower frequency UWB radar in the TWI scenario. In addition, for the quantitative comparison of the conventional STFT-based Doppler velocity estimation methods, the local maximum points in the range-Doppler velocity map shown in Fig. 4 are regarded as being the estimated Doppler velocity values. Under these evaluation conditions, the cumulative probability satisfying $e_{v_d}(v_{d,i}^{\mathrm{est}}) < 0.02$ m/s and RMSEs between the STFT-based and the proposed method are summarized in Table I. This comparison verified the effectiveness of the accuracy of the Doppler velocity estimation in the proposed method.

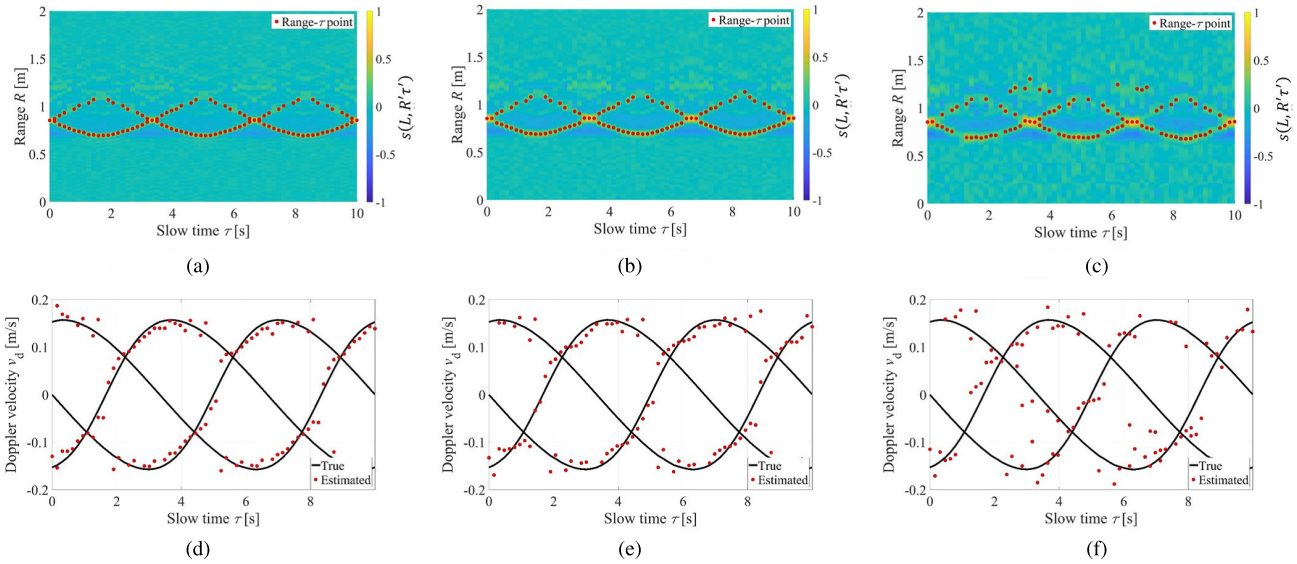

Fig. 7. Responses of filter and extracted range–τ points for (a) S/N = 30 dB, (b) S/N = 20 dB, and (c) S/N = 10 dB. Estimated Doppler velocities (red solid circles) by the proposed method at case 2 in (d) S/N = 30 dB, (e) S/N = 20 dB, and (f) S/N = 10 dB.

TABLE I
ERROR ANALYSIS AS CUMULATIVE PROBABILITY FOR $\mathrm{Err}_{\mathrm{Range}} \leq 0.02$ m/s AND RMSE FOR EACH METHOD

	$e_{v_d} \leq 0.02$ m/s		RMSE	
	STFT	Proposed	STFT	Proposed
Case 1	55.0 %	79.5 %	0.070 m/s	0.035 m/s
Case 2	40.0 %	84.6 %	0.021 m/s	0.019 m/s
Case 3	39.1 %	67.3%	0.029 m/s	0.027 m/s

3) Noisy Scenario: This section investigates the sensitivity to additive random noise in the proposed Doppler velocity estimation. The same observation model assumed in the previous section, described in Section IV-A, is assumed. The white Gaussian noise is directly added to the recorded electric field at each antenna. The signal-to-noise ratio (S/N) is defined as the ratio of the peak intensity to the average noise power in the range-Doppler data with nonzero Doppler velocity. Note that, this definition of S/N is the strictest criterion among other S/N definitions, because the S/N is calculated after applying the matched filter, which is the most noise-robust filter. This definition, thus, considers the locality of the signal in both the time and frequency domains, and the situation that S/N exceeds 30 dB is possible in a realistic scenario, has been experimentally demonstrated [24], [25]. case 2 (three targets) is selected in this test. Fig. 7(a)–(c) shows the range–τ responses and the extracted range points for S/Ns of 30, 20, and 10 dB. Fig. 7(d)–(f) shows the results of the estimated Doppler velocities along the slow-time direction, obtained using the proposed method for each S/N level. The plots show that there are no significant differences between the results for S/N of 20 and 30 dB and the results for the noiseless case, revealing the noise robustness of the proposed method. Meanwhile, for S/N = 10 dB, we see a number of falsely detected range–τ points in Fig. 7(c), possibly resulting in false target detection. However, by assessing the evaluation function in (2), we can threshold out these kinds of false points, as shown in Fig. 7(f). As a quantitative error analysis, the cumulative probabilities satisfying $e_{v_d}(v_{d,i}^{\mathrm{est}}) < 0.02$ m/s is 82.6% for the case of SNR = 30 dB, 79.6% for the case of SNR = 20 dB, and 57.7% the case of SNR = 10 dB, where the nominal Doppler velocity resolution in Fig. 4 is 0.04 m/s. The above results demonstrate the robustness of the proposed method against additive noise.

4) Sensitivity Study for Parameters: The performance of the proposed method depends on the parameters used in (2): σ_{v_d}, σ_s, and σ_τ. A sensitivity analysis for these parameters of the proposed method is conducted as follows. Figs. 8 and 9 show the cumulative probabilities of the estimation errors for the Doppler velocity at different σ_{v_d} and σ_τ values, where case 2 (three targets) is chosen as the representative noiseless case. Fig. 8 demonstrates that there is no serious sensitivity as to σ_τ, which expresses the correlation length along the slow-time direction. It is considered that a longer correlation length for σ_τ results in inaccuracy around the start or end snapshot in the pulse hits, while a shorter σ_τ is sensitive to small fluctuation of extracted ranges. Fig. 9 shows that σ_{v_d} should be greater than a certain value to maintain the accuracy ($\sigma_{v_d} = 0.02$ m/s in this case), suggesting that the correlation length should be longer than the fluctuation in the calculated Doppler velocities $v_{d,i,j}$. We also confirm that there is no severe sensitivity in terms of σ_s, which is regarded as being the variation in the strength of each reflection response due to a propagation loss or reflection surface. Furthermore, this must be larger than 0.1 to allow for 10% variations in the reflection strength during multiple pulse hits.

B. Experimental Test

This section describes the experimental validation of the proposed Doppler velocity estimation method, using UWB radar equipment, assuming a free-space imaging scenario, for simplicity. Fig. 10 shows the measurement setup using UWB impulse radar produced by the Sakura Tech Corporation. The impulse UWB radar has an 8.5-GHz center frequency (35.3-mm wavelength) and a 1.5-GHz 10-dB bandwidth.

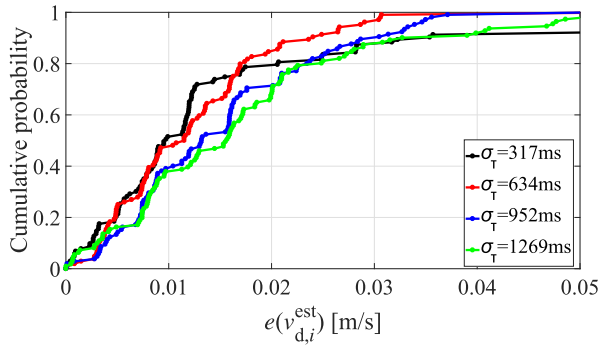

Fig. 8. Cumulative probability of the errors for different parameters of σ_τ in the proposed method in case 2, where $\sigma_{v_d} = 0.04$ m/s and $\sigma_s = 0.7$ are fixed.

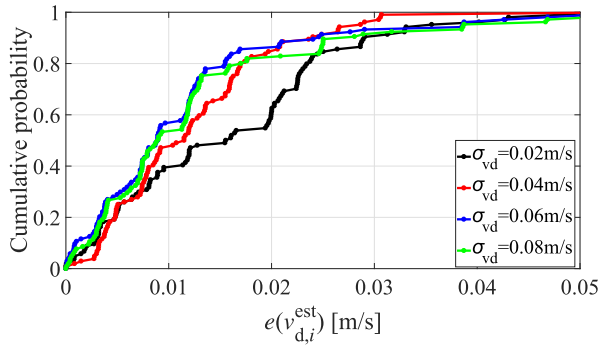

Fig. 9. Cumulative probability of the errors for different parameters of σ_{v_d} in the proposed method in case 2, where $\sigma_\tau = 634$ ms and $\sigma_s = 0.7$ are fixed.

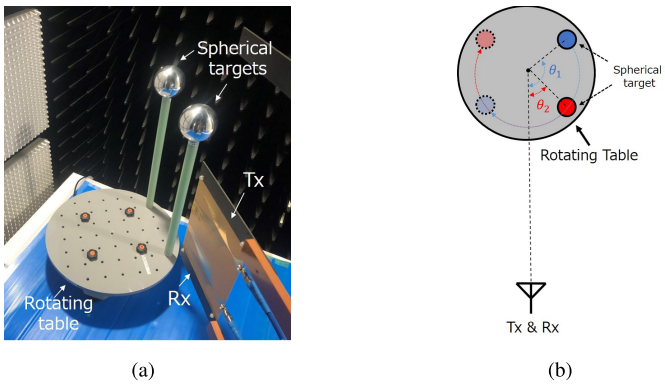

Fig. 10. Experimental setup, including two spherical targets with rotating table and the transmitting and receiving Fermi antennas. (a) Photograph. (b) Geometrical arrangement.

That is, the theoretical range resolution is 100 mm. The transmitting and receiving broadband Fermi antennas are arranged vertically separated by 100 mm. Both E- and H-plane 3-dB beamwidths of the Fermi antennas are 40°. Fig. 11 shows the power spectrum of the transmitting pulse. The two spherical targets, each with a diameter of 100 mm, are rotated by an azimuth table with an accuracy of 0.1° and a rotational speed of 0.5π m/s, being the same conditions as those in the numerical simulation case. Stop-and-go observations for each rotation angle were performed to obtain an accurate profile of the actual range and Doppler velocity, where the angle of rotation θ is assumed to be $0 \le \theta \le \pi$ with $\pi/36$ spacing, that is, 37 observations (pulse hits) are acquired. The distance from

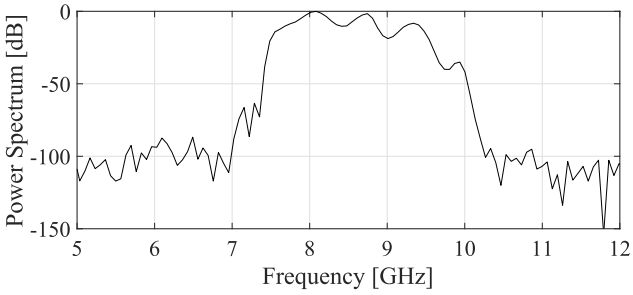

Fig. 11. Power spectrum of transmitting signal in the experiment.

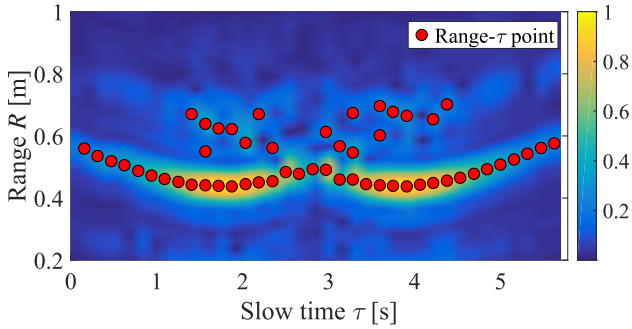

Fig. 12. Envelope response of the matched filter and extracted range–τ points (red solid circle) in the experiment. Color: strength of signals.

the radar unit to the center of the rotation table is 475 mm and that from each target to the rotation center is 217 mm. Here, the PRI is 156.25 ms, which is almost the same as in the simulation. The range of the unambiguous Doppler velocity is $|v_d| < 0.0575$ m/s, which is determined by the center frequency and the PRI. The number of pulse hits is 37 and the total observation time is 5.625 s. Fig. 12 shows the received data after applying the matched filter as well as the extracted range points. The figure demonstrates that the response from each target can be observed, while part of the response is lost due to the shadowing effect. Fig. 13 shows the results of the STFT analysis, that is, the traditional method wherein the temporal window along the slow-time direction is 1.25 s, corresponding to a nominal Doppler velocity resolution of 0.0141 m/s in this case. As shown in Fig. 13, the STFT-based method could not identify a significant response for the Doppler velocity, which varies greatly over the PRI. This is because the range of the unambiguous Doppler velocity in the STFT method, calculated as $|v_d| < 0.0575$ m/s, is considerably smaller than that of the actual Doppler velocity variation as $|v_d| > 0.1$ m/s. Then, the STFT analysis suffers from inaccuracy due to the ambiguity responses as in Fig. 13. In addition, the temporal resolution of 1.25 s is obviously insufficient compared with the temporal variation of the actual Doppler velocity. As a higher temporal resolution case, Fig. 14 shows the results of the STFT analysis using the temporal window with 0.625 s, corresponding to a nominal Doppler velocity resolution of 0.0282 m/s. As shown in Fig. 14, the STFT responses suffer from a lower Doppler velocity resolution in return for higher temporal resolution. On the contrary, Fig. 15 shows the results of the Doppler velocity estimation obtained using the proposed method, where the parameters are set to $\sigma_s = 0.7$, $\sigma_{v_d} = 0.04$ m/s, and

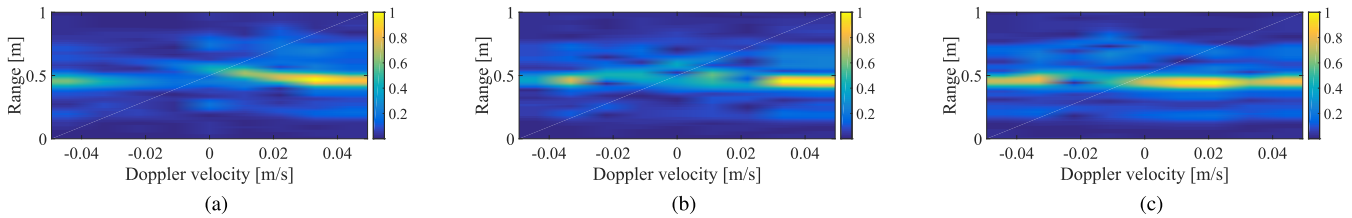

Fig. 13. Range-Doppler velocity responses by the STFT-based analysis with the temporal window width of 1.25 s. All actual Doppler velocities in each case are out of the range of unambiguous Doppler velocity. (a) 0.15 s $\leq \tau \leq$ 1.40 s. (b) 2.03 s $\leq \tau \leq$ 3.28 s. (c) 3.90 s $\leq \tau \leq$ 5.15 s.

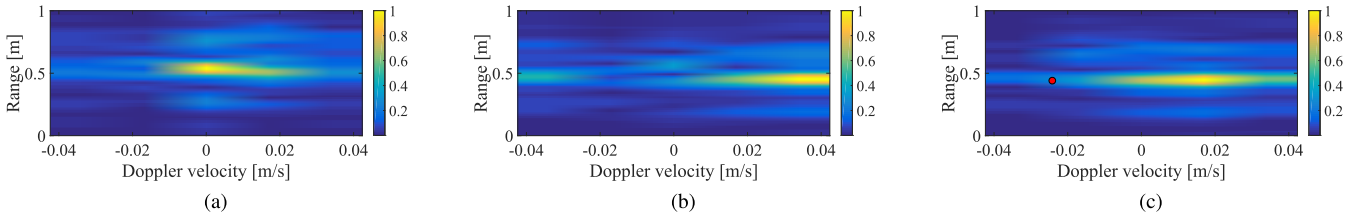

Fig. 14. Range-Doppler velocity responses by the STFT-based analysis with the temporal window width of 0.625 s. One actual Doppler velocity (red solid circles) in (c) is within the range of unambiguous Doppler velocity. (a) 0.15 s $\leq \tau \leq$ 0.775 s. (b) 2.03 s $\leq \tau \leq$ 2.655 s. (c) 3.90 s $\leq \tau \leq$ 4.525 s.

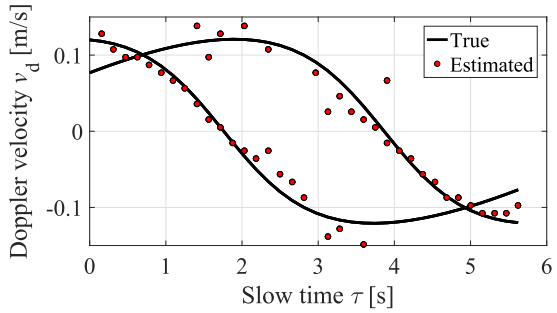

Fig. 15. Estimated Doppler velocities (red solid circles) by the proposed method using the experimental data in the cases without wall, where the two spherical targets are rotated.

$\sigma_\tau = 625$ ms, these being almost the same as in the simulation. Fig. 15 shows that our proposed method provides an accurate Doppler velocity estimation, even when the range of the unambiguous Doppler velocity in the STFT does not cover the actual Doppler velocity variations, because each Doppler velocity is determined by the group of the inclinations of the range–τ points in the proposed method, and this is another advantage for the proposed method, especially in assuming large PRI. The RMSE for the Doppler velocity estimation is 0.019 m/s, which is smaller than the Doppler resolution in the above STFT analysis in assuming higher temporal resolution case, as in Fig. 14. Note that it is sometimes impossible to acquire an estimate as a result of the shadowing effect or the strong interference between the two targets with almost the same ranges, as can be observed in the simulation results shown in Fig. 5.

V. Application Examples for 3-D Human Body Imaging Scenario

This section describes the incorporation of the Doppler velocity estimation method, proposed in Section III, into 3-D human body imaging to emphasize the advantages of the proposed method. The super-resolution property of the proposed Doppler velocity estimation motivates the incorporation of a promising signal processing and imaging algorithm. We here focus on the CS-based TOA estimation as the range–τ points' extraction and the RPM imaging algorithm for the 3-D imaging scenario assuming a human body with micro-Doppler variations. We briefly introduce each methodology and incorporate these algorithms for the actual human body imaging scenario as follows.

A. RPM Method

The RPM method was originally developed in [19] and has been extended to various observation models [2], [21], [22]. This method assumes that a target boundary point exists on a spheroid with focal points $\boldsymbol{L}_\mathrm{T}$ and $\boldsymbol{L}_\mathrm{R}$ and major radius R, which are given by the so-called range points or range–τ points denoted by $\boldsymbol{q}$. The scattering center $\hat{\boldsymbol{p}}(\boldsymbol{q}_i)$ corresponding to range point $\boldsymbol{q}_i$ (called MainRP) is determined by assessing the spatial accumulation of intersection points calculated using other range points (called SubRPs) as

$$\hat{\boldsymbol{p}}(\boldsymbol{q}_i) = \underset{\boldsymbol{p}^{\mathrm{int}}(\boldsymbol{q}_i;\boldsymbol{q}_l,\boldsymbol{q}_m)\in\mathcal{P}_i}{\arg\max} \sum_{(\boldsymbol{q}_j,\boldsymbol{q}_k)\in\mathcal{Q}_{\mathrm{all}}} g(\boldsymbol{q}_i;\boldsymbol{q}_j,\boldsymbol{q}_k) \times \exp\left\{-\frac{||\boldsymbol{p}^{\mathrm{int}}(\boldsymbol{q}_i;\boldsymbol{q}_j,\boldsymbol{q}_k)-\boldsymbol{p}^{\mathrm{int}}(\boldsymbol{q}_i;\boldsymbol{q}_l,\boldsymbol{q}_m)||}{2\sigma_r^2}\right\} \tag{4}$$

where $p^{\mathrm{int}}(\boldsymbol{q}_i;\boldsymbol{q}_j,\boldsymbol{q}_k)$ denotes the intersection points of three spheroids, whose focii are the positions of the transmitting and receiving antennas and whose major radius is R. $\mathcal{P}_i$ denotes a set of these intersection points and σ_r is determined considering the spatial density of the accumulated intersection points. $\mathcal{Q}_{\mathrm{all}}$ is the set of all range points. The weighting function $g(\boldsymbol{q}_i;\boldsymbol{q}_j,\boldsymbol{q}_k)$ is defined as

$$g(\boldsymbol{q}_i;\boldsymbol{q}_j,\boldsymbol{q}_k) = s(\boldsymbol{q}_j)\exp\left\{-\frac{D(\boldsymbol{q}_i,\boldsymbol{q}_j)}{2\sigma_D^2}\right\} + s(\boldsymbol{q}_k)\exp\left\{-\frac{D(\boldsymbol{q}_i,\boldsymbol{q}_k)}{2\sigma_D^2}\right\} \tag{5}$$

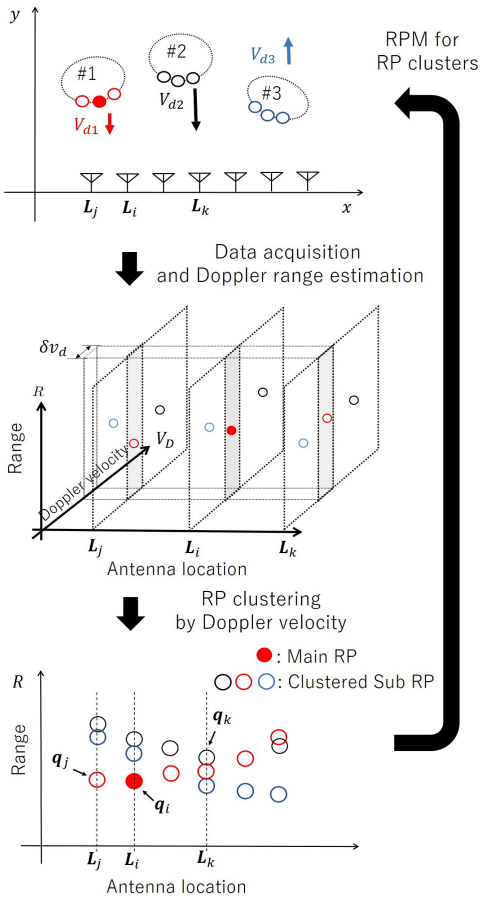

Fig. 16. Range points' clustering based on Doppler velocity discrimination as the preprocess of the RPM method.

where σ_D is determined empirically and $D(\boldsymbol{q}_i, \boldsymbol{q}_j)$ denotes the actual separation of the two sets of transmitting and receiving antennas and is expressed as

$$D(\boldsymbol{q}_i, \boldsymbol{q}_j) = \min(\|\boldsymbol{L}_{\mathrm{T},i} - \boldsymbol{L}_{\mathrm{T},j}\|^2 + \|\boldsymbol{L}_{\mathrm{R},i} - \boldsymbol{L}_{\mathrm{R},j}\|^2, \|\boldsymbol{L}_{\mathrm{T},i} - \boldsymbol{L}_{\mathrm{R},j}\|^2 + \|\boldsymbol{L}_{\mathrm{R},i} - \boldsymbol{L}_{\mathrm{T},j}\|^2). \quad (6)$$

Note that, in (4), the optimal combination of $\boldsymbol{q}_l$ and $\boldsymbol{q}_m$ is determined by fully searching for all possible combinations.

Many reports have revealed that the RPM has a number of advantages over the coherent-based imaging methods, such as SAR or beamforming, that it maintains the reconstruction accuracy, even assuming sparse array configuration (more than a half of wavelength) due to incoherent process, and also it has another advantage that data association with polarimetric data [22] or Doppler velocity data [2] is achieved using one-to-one correspondence between the range point $\boldsymbol{q}_i$ and the scattering center $\hat{\boldsymbol{p}}(\boldsymbol{q}_i)$. However, in the presence of multiple objects, the greater number of SubRPs explosively increases the computational cost because it is necessary to calculate the intersection points of the three spheroids among all possible SubRPs' combinations, which must be solved numerically. In addition, the combination of MainRP and SubRPs' points from different targets introduces inaccuracy in the calculation of the actual scattering point in (4).

The clustering scheme of SubRPs for each MainRP offers a promising solution to the above issues, because the SubRPs should be included in the same target cluster of the MainRP. In other words, if the MainRP is caused from the kth target, it should be processed using only the SubRPs from the kth target. Fig. 16 shows the concept of RP clustering before the RPM process. The observation data are processed and converted to a range-Doppler velocity map for each antenna combination, and after the SubRPs' clustering for each MainRP considering the Doppler velocity proximity, the RPM is applied only for each clustered SubRP. A previous study [2] introduced Doppler velocity-based range points' clustering to appropriately cluster SubRPs for each MainRP without *a priori* information on the target shape. The methodology and procedure have been described [2], and the effectiveness of the method has been demonstrated assuming a 140-GHz millimeter radar system. However, in the lower band UWB radar scenario, the Doppler velocity resolution becomes considerably worse than that obtained by the above millimeter-wave radar system, and it is difficult to apply the above clustering scheme. We thus introduce the proposed Doppler estimation algorithm in Section III-A to obtain a sufficient resolution and accuracy in Doppler velocity estimation with higher temporal resolution.

B. CS Filter-Based Range Point Extraction

The other problem with the lower band UWB radar is lower range resolution because it is not possible to obtain a frequency band as wide as that of the millimeter radar system, mostly due to limited antenna characteristics or legal regulations (e.g., the spectrum mask of the emission level [23]). Thus, to take full advantage of RPM imaging, the super-resolution range extraction filter is introduced, the advantage of which has been demonstrated in the literature [24]. The CS-based approach is a promising solution to obtain higher range resolution without ambiguity responses. The CS filter assumes that the actual range profile satisfies a sparse representation, which is mostly a reasonable assumption in the radar scenario. Let $\boldsymbol{x}$ be the object range profile, $\boldsymbol{n}$ be a noise component, and $\boldsymbol{s}$ be the received signal, all of which are discretely sampled with a sufficiently small interval. Here, the object range profile $\hat{\boldsymbol{x}}$ is determined as the solution to an optimization problem

$$\hat{\boldsymbol{x}} = \arg\min_{\boldsymbol{x}} \left(\|\boldsymbol{s} - \boldsymbol{A}\boldsymbol{x}\|_2^2 + \lambda_{\mathrm{CS}}\|\boldsymbol{x}\|_1\right) \quad (7)$$

where $\boldsymbol{A}$ denotes the observation matrix defined as in (8), at the bottom of the next page. Here, $\boldsymbol{h} = (h(0), \ldots, h(K))$ denotes the impulse response of a transmitted pulse, and K denotes the maximum length of $\boldsymbol{h}$. Note that, to achieve a super-resolution and highly accurate range profile production, an oversampling process is usually required, which can be easily achieved by using a zero-padding scheme for the higher frequency areas in the frequency domain, if the Nyquist criteria would be satisfied.

The procedure, incorporating the proposed method, CS-based filter, and Doppler associated RPM, is summarized as follows.

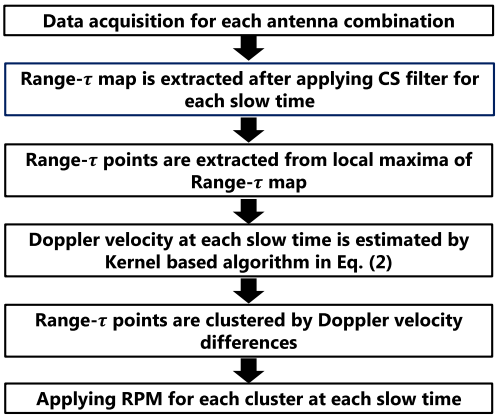

Fig. 17. Flowchart of incorporating the proposed method, CS-based filter, and the Doppler associated RPM.

TABLE II

DOPPLER VELOCITIES FOR EACH PART OF HUMAN BODY

Doppler velocity	Parts
0.5 m/s	Right lower arm & Left lower leg
1.0 m/s	Right upper arm & Left upper leg
1.5 m/s	Head & Lower and Upper torso
2.0 m/s	Left upper arm & Right upper leg
2.5 m/s	Left lower arm & Right lower leg

Step 1: Received signals are recorded and each range profile is calculated by CS filtering according to (7) at each slow time τ, which is denoted as $s(\boldsymbol{L}_{\mathrm{T}}, \boldsymbol{L}_{\mathrm{R}}, R', \tau')$.

Step 2: Range–τ points $\boldsymbol{q}$ are extracted from the set of local maxima of $s(\boldsymbol{L}_{\mathrm{T}}, \boldsymbol{L}_{\mathrm{R}}, R', \tau')$.

Step 3: Optimal Doppler velocity $\hat{v}_{d,i}$ is obtained using (2) for each $\boldsymbol{q}$.

Step 4: Range–τ points are clustered by the Doppler velocity, where the proximity of the Doppler velocity between $\boldsymbol{q}_i$ and $\boldsymbol{q}_j$ is defined as

$$\delta v_d(\boldsymbol{q}_i, \boldsymbol{q}_j) \equiv |v_{d,i} - v_{d,j}|. \tag{9}$$

A set of SubRPs (RP cluster for $\boldsymbol{q}_i$) satisfies $\delta v_d(\boldsymbol{q}_i, \boldsymbol{q}_j) \leq \delta v_{d,\mathrm{th}}$ and is denoted as $\mathcal{Q}_i$.

Step 5: $\boldsymbol{q}_i$ is converted to a target point $\hat{\boldsymbol{p}}(\boldsymbol{q}_i)$ by RPM using $\mathcal{Q}_i$ in (4).

Step 6: For each target point $\hat{\boldsymbol{p}}(\boldsymbol{q}_i)$, the Doppler velocity $v_{d,i}$ is associated.

Fig. 17 shows the flowchart of the above procedure.

C. Numerical Test for Human Body Imaging

1) Numerical Setting: As a promising application of the proposed Doppler velocity estimation method, this section introduces a numerical test for its incorporation with CS-based TOA estimation and RPM-based imaging, assuming human body imaging scenario. For simplicity, the front wall is not considered here. The transmitting signal forms a Gaussian-modulated sinusoidal pulse, where the center frequency is 5.0 GHz corresponding to the center wavelength of $\lambda = 60$ mm, and the effective bandwidth is 3.0 GHz, whose theoretical range resolution in air is 50 mm. The PRI is 20.0 ms, while the number of pulse hits is 10. The total observation time is $T_c = 0.2$ s, and thus, in the sense of Fourier transform-based analysis, the lower limit of the Doppler velocity resolution is 0.15 m/s using the center wavelength. Fig. 18 shows the observation model and the assumed human body object in this case. It is assumed that the target is a human body approximated as an aggregation of 11 ellipsoids corresponding to the head, upper and lower torsos, arms, and legs, for simplicity. For simplicity, we consider the stepping motion of human body at the same position with the motion vector along the y-axis, which is summarized as in Table II. In this case, each motion velocity is set constant in any slow-time snapshot, for simplicity. The 4 transmitting and 25 receiving antennas are arranged on square planar arrays with the spacing of 50 mm (5/6 λ), where a transmitter is set to each vertex of the square array. Note that, the above array configuration would generate a false image when the coherent-based SAR or beamforming process is applied, because the minimum spacing of array is more than a half of wavelength. Received data with all combinations for $\boldsymbol{L}_{\mathrm{T}}$ and $\boldsymbol{L}_{\mathrm{R}}$ are processed, i.e., the MIMO radar model is assumed. The received time-series data are generated by geometrical optics (GO) approximation without the consideration of multiple scattering among targets. The GO is the forward solver based on higher frequency approximation, where the dominant propagation path can be determined by the law of reflection in optics [26]. The reason for introducing the GO based data generation is that it requires

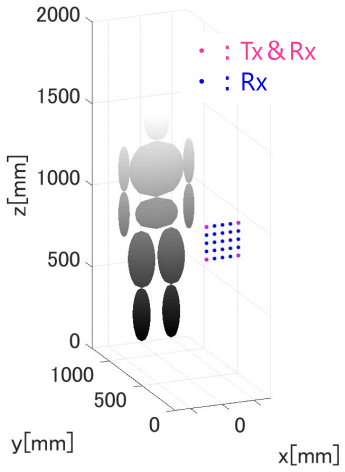

Fig. 18. Observation model and human body setting in numerical test.

$$\boldsymbol{A} \equiv \begin{pmatrix} h(K), & h(K-1), & \ldots, & h(0), & 0, & 0, & \ldots, & 0, \\ 0, & h(K), & \ldots, & h(1), & h(0), & 0, & \ldots, & 0, \\ & & & \ddots & & & & \\ 0, & 0, & \ldots, & 0, & h(K), & h(K-1), & \ldots, & h(0), \end{pmatrix}. \tag{8}$$

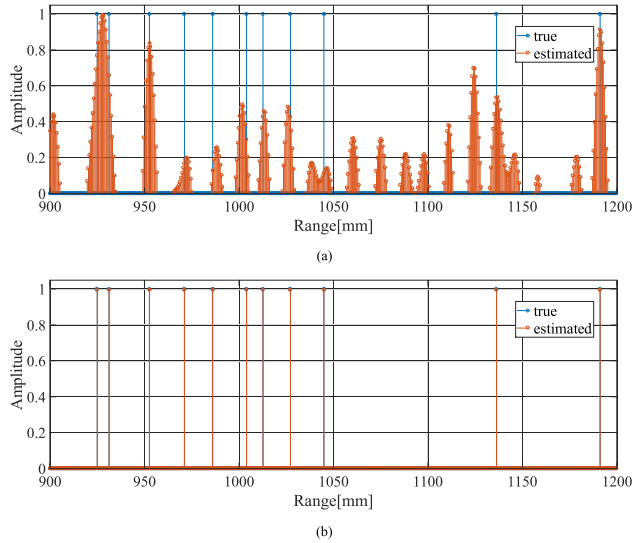

Fig. 19. Example of range profile responses (red lines) by (a) Wiener filter and (b) CS filter, where the actual ranges are as blue solid lines.

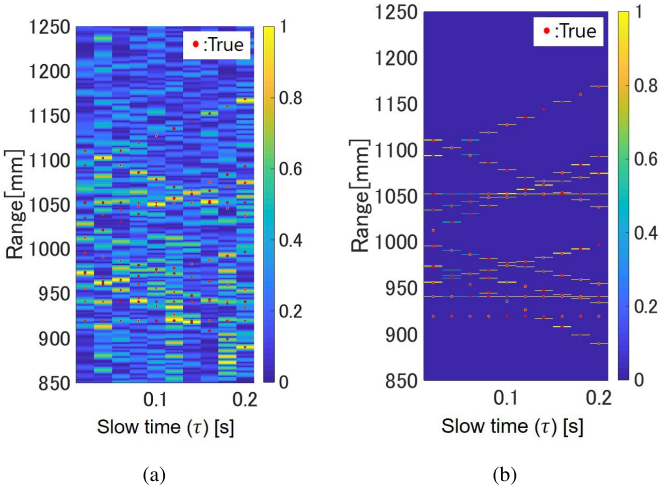

Fig. 20. Range–τ distribution obtained by (a) Wiener filter and (b) CS filter, where the color denotes a strength of each response. Red points: actual range–τ points.

much less computational cost compared with other forward solver, compared with the 3-D FDTD method, and we deal with smoothed surface target, the curvature radius of each part of human body is enough larger than the assumed center wavelength (60 mm). The noiseless case is assumed here to evaluate only a systematic error for each method.

2) Results and Discussion: First, to clarify the effectiveness of the CS-based range (TOA) estimation, Fig. 19 shows one example of range responses obtained by the conventional Wiener filter (detailed in [2] and [19]) and CS filter, where the number of the pulse hit is 5 (i.e., $\tau = 0.1$ s) at $\boldsymbol{L}_{\mathrm{T}} = (-100, 0, 1100)$ and $\boldsymbol{L}_{\mathrm{R}} = (0, 0, 950)$. Here, $\lambda_{\mathrm{CS}} = 10^{-3}$ is set in (7), which is empirically determined in investigating a number of similar examples. Also, Fig. 20 shows the range–τ responses by each filter, and the extracted range–τ points at the same antenna combination in Fig. 19. These figures demonstrate that the Wiener filter-based range estimation suffers from inaccuracy due to numerous range sidelobe responses, which

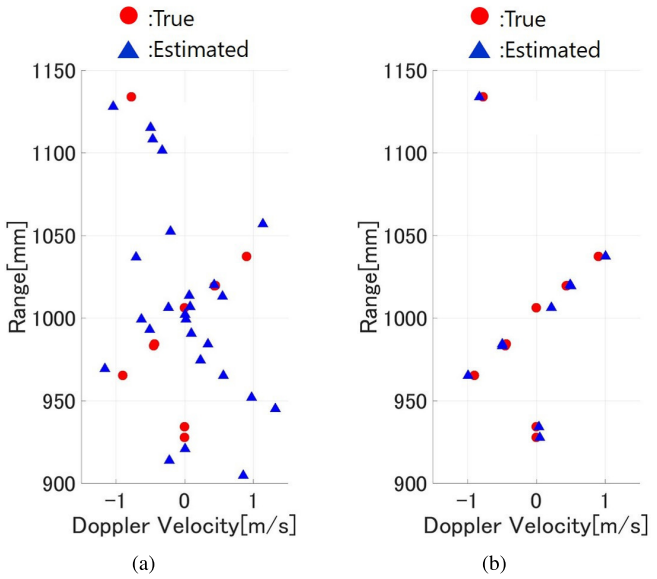

Fig. 21. Range-Doppler velocity estimation examples by (a) Method-I [2] and (b) Method-II. Red solid circles and blue solid triangles denote the actual and estimated range-Doppler points, respectively.

leads to many false detections of the range points. In contrast, the CS filter considerably enhances the accuracy and resolution of range estimation by efficiently suppressing the sidelobe effect with sparse regularization. Second, the performance of Doppler estimation, in this case, is investigated. Here, the conventional method uses the Fourier transform-based Doppler velocity estimation from the Wiener filter responses as in Fig. 20(a), and we call the method as "Method-I." On the other hand, "Method-II" employs the Gaussian kernel-based Doppler velocity estimation from the CS filter responses as in Fig. 20(b). As shown in this figure, the CS filter offers an accurate and higher range resolution; however, the extremely impulsive form of range profile, like that shown in Fig. 20(b), gives rise to a new problem in that the RW effects could be more severe, because the extremely narrower pulses (not having a carrier frequency) would be provided by the CS filter, where the neighboring pulses would hardly overlap along the slow-time direction. Therefore, the coherent integration-based Doppler velocity estimation, including the higher resolution time–frequency analyses such as [13]–[16], could not offer a meaning results for Doppler velocity estimation, because they require at least two pulses (with carrier frequency) within the same range resolution to apply the coherent integration process. Table III summarizes the contents of the above methods. Fig. 21 denotes one example of the range-Doppler estimation results at the fixed antenna combination. Here, $\sigma_s = 0.7$, $\sigma_{v_d} = 0.4$ m/s, and $\sigma_\tau = 100$ ms are set in (2). As in Fig. 21(a), Method-I seriously suffers from inaccuracy for both range and Doppler velocity estimations, because the Wiener filter responses could generate false range peaks and the Fourier-based analysis is not suitable for the case that target range responses are not overlapped along the slow-time direction, and has a lower limit of Doppler velocity resolution. On the contrary, Fig. 21(b) denotes that "Method-II" achieves accurate range and Doppler velocity estimations in

TABLE III
CONTENTS OF EACH METHOD

	Method-I	Method-II
Range extraction filter	Wiener filter	CS filter
Doppler velocity estimation	Fourier based	Kernel based (Proposed)
Imaging algorithm	RPM w Doppler clustering	RPM w Doppler clustering

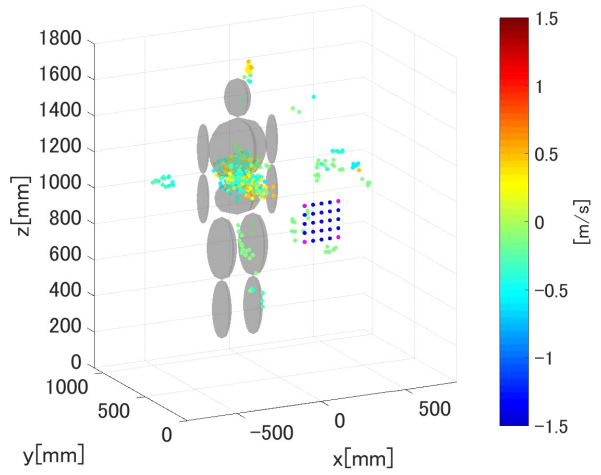

Fig. 22. Scattering center points obtained by Method-I [2] in noiseless case. Color bar denotes the estimated Doppler velocity for each estimated point.

such richly interfered cases because the proposed Gaussian kernel-based method exploits the notable feature of the CS filter (very higher range resolution), while the Fourier- or STFT-based analysis hardly deals with such impulsive (quite wider fractional bandwidth) responses by the CS filter. Note that, while Fig. 21(a) denotes the average responses along slow-time direction, Fig. 21(a) illustrates the instantaneous response at the one pulse hit (one snapshot of slow time), which means that quite higher temporal resolution is available in Method-II.

For quantitative analysis, we introduce the Doppler velocity error as $e_{v_d}(v_{d,i}^{\mathrm{est}})$, which is defined in (3). Also, the range error is similarly defined as

$$e_{\mathrm{R}}(R_i^{\mathrm{est}}) \equiv \min_{R^{\mathrm{true}}} \left| R_i^{\mathrm{est}} - R^{\mathrm{true}} \right|, \quad (i = 1, 2, \ldots, N_{\mathrm{T}}) \tag{10}$$

where R_i^{est} is the estimated range of the ith range–τ point $\boldsymbol{q}_i$, R^{true} are the true ranges at each slow-time snapshot, and N_{T} is the total number of R_i^{est}. Using the above error definition, Table IV summarizes the cumulative probabilities in satisfying each error criteria for range and Doppler velocity in each method. The table quantitatively demonstrates the effectiveness of Method-II in terms of accurate range and Doppler estimation performance.

Finally, the 3-D imaging performance obtained by the RPM method is presented. Fig. 22 shows the RPM image using the range points by the conventional method, i.e., the Fourier-based Doppler analysis with Wiener filter responses [2]. As shown in Fig. 22, the RPM imaging points obtained with Method-I [2] seriously deviate from the actual ellipsoid surface because of the lower accuracy and resolution for range point and Doppler velocity due to richly interfered situations. In contrast, Fig. 23 shows the RPM image using the range

TABLE IV
CUMULATIVE PROBABILITIES SATISFYING EACH ERROR CRITERION OF RANGE AND DOPPLER VELOCITY FOR EACH METHOD

Error range	Method-I [2]	Method-II
$\lvert e_{v_{\mathrm{d}}} \rvert \leq 0.1$ m/s, $\lvert e_{\mathrm{R}} \rvert \leq 10$ mm	2.5 %	34.5 %
$\lvert e_{v_{\mathrm{d}}} \rvert \leq 0.2$ m/s, $\lvert e_{\mathrm{R}} \rvert \leq 10$ mm	8.0 %	60.1 %
$\lvert e_{v_{\mathrm{d}}} \rvert \leq 0.2$ m/s, $\lvert e_{\mathrm{R}} \rvert \leq 20$ mm	15.2 %	68.7 %

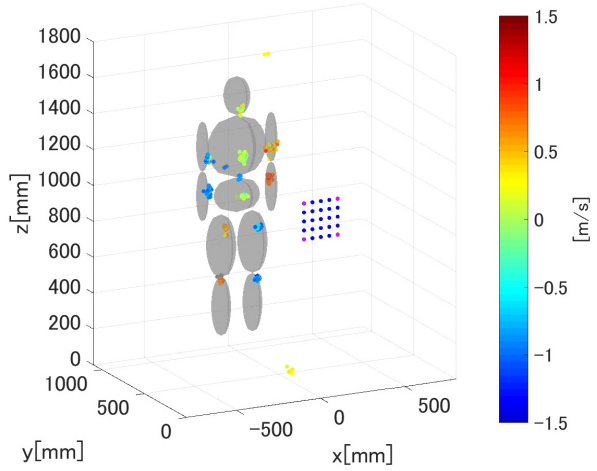

Fig. 23. Scattering center points obtained by Method-II in noiseless case. Color bar denotes the estimated Doppler velocity for each estimated point.

points by Method-II, i.e., the proposed kernel-based Doppler analysis with CS filter responses. Here, the snapshot at the fifth pulse hit ($\tau = 0.1$ s) is presented. In contrast, Method-II as in Fig. 23 offers an accurate boundary or each part of the human-mimicking ellipsoids, resulting from the upgrade of RP estimation through CS and the enhancement of the Doppler estimation through the proposed kernel-based method. For the quantitative evaluation, the reconstruction error denoted by $e_{\mathrm{image}}(\boldsymbol{p}_i^{\mathrm{est}})$ is introduced as

$$e_{\mathrm{image}}\left(\boldsymbol{p}_i^{\mathrm{est}}\right) = \min_{\boldsymbol{p}^{\mathrm{true}}} \left\| \boldsymbol{p}_i^{\mathrm{est}} - \boldsymbol{p}^{\mathrm{true}} \right\|_2, \quad (i = 1, 2, \ldots, N_{\mathrm{T}}) \tag{11}$$

where $\boldsymbol{p}_i^{\mathrm{est}}$ and $\boldsymbol{p}^{\mathrm{true}}$ are, respectively, the locations of the ith estimated point and the true target point (i.e., the group of discretized points on the ellipsoid surface with a sufficiently dense sample in this case), and N_{T} is the total number of $\boldsymbol{p}_i^{\mathrm{est}}$. The numbers of reconstructed points satisfying $e_{\mathrm{image}} <$ 10 mm ($=1/6\lambda$) are 286 [13.2% of all points (2123)] for the image in Fig. 22 (Method I) and 465 [79.3% of all points (586)] for the image in Fig. 23 (Method II), and it shows that the accuracy obtained by the proposed incorporation algorithm is remarkably higher compared with the method based on the literature [2].

VI. CONCLUSION

This article proposed super-resolution Doppler velocity estimation based on the kernel density estimator assuming the UWB-TWI scenario. The traditional analysis based on the Fourier transform suffers from lower Doppler and temporal resolutions due to the RW effect and time-variant Doppler velocity feature in the UWB lower frequency band radar. To overcome the above difficulty, this article newly introduces

the Gaussian kernel-based algorithm for conversion from measured range–τ points to Doppler velocity points without any connecting or tracking procedures. While the proposed idea of range–τ conversion was inspired by the algorithm of the RPM method, the proposed method relies on Doppler velocity estimation, which is totally different from the issue faced with RPM, namely, the 3-D imaging scenario. It should also be noted that the proposed method further resolves the tracking problem encountered in time-variant Doppler velocity estimation issued in [17] and has numerous other advantages in terms of Doppler velocity resolution, temporal resolution, unambiguity in velocity estimation, and applicability to time-variant, multiobjects cases while being based on a tracking-free algorithm. In addition, to achieve the best performance in 3-D human body imaging, the CS-based TOA estimation and the proposed Kernel-based Doppler velocity estimation are appropriately incorporated in the framework of Doppler clustering-based RPM imaging. The 2-D FDTD-based numerical simulation of a UWB-TWI scenario and the experimental validation, assuming free-spacing imaging with the actual Impulse UWB radar system, demonstrated that the proposed method can be used for accurate motion vector estimation with considerably higher temporal resolution on the order of the PRI, which cannot be achieved using traditional algorithms. Note that, the proposed method is not based on a coherent integration process but employs a procedure for connecting the range–τ points, which are extracted from the local maxima of the filter output. While such a connecting problem is not easy to solve when there are many scattering points, the stochastic kernel-based approach provides a robust solution to this problem, while a similar problem has been effectively resolved by the RPM method. Finally, the 3-D GO-based simulation, assuming human-mimicking objects, verified that our proposed method remarkably enhances the reconstruction accuracy for each part of the human body, even when using lower frequency band radar. It is noted that the proposed method provides an RPM image for each slow-time snapshot, because the range-Doppler data are available for each slow time τ (i.e., each pulse sequence), and the RP clustering scheme is effective for each snapshot. In contrast, a coherent integration scheme such as the Fourier transform only provides the time-averaged Doppler velocity and image. The above point is a critical advantage of the proposed method.

REFERENCES

[1] D. Bujaković, M. Andrić, B. Bondžnulić, and D. Mikluc, "Analysis of human radar echo signal using warped discrete Fourier transform," *New Trends Signal Process. (NTSP)*, Oct. 2016, pp. 1–6.

[2] Y. Sasaki, F. Shang, S. Kidera, T. Kirimoto, K. Saho, and T. Sato, "Three-dimensional imaging method incorporating range points migration and Doppler velocity estimation for UWB millimeter-wave radar," *IEEE Geosci. Remote Sens. Lett.*, vol. 14, no. 1, pp. 122–126, Jan. 2017.

[3] Z. Sun, X. Li, W. Yi, G. Cui, and L. Kong, "Range walk correction and velocity estimation for high-speed target detection," in *Proc. IEEE Radar Conf.*, May 2017, pp. 1478–1482.

[4] B. D. Carlson, E. D. Evans, and S. L. Wilson, "Search radar detection and track with the Hough transform. I. System concept," *IEEE Trans. Aerosp. Electron. Syst.*, vol. 30, no. 1, pp. 102–108, Jan. 1994.

[5] B. D. Carlson, E. D. Evans, and S. L. Wilson, "Search radar detection and track with the Hough transform. II. Detection statistics," *IEEE Trans. Aerosp. Electron. Syst.*, vol. 30, no. 1, pp. 109–115, Jan. 1994.

[6] B. D. Carlson, E. D. Evans, and S. L. Wilson, "Search radar detection and track with the Hough transform. III. Detection performance with binary integration," *IEEE Trans. Aerosp. Electron. Syst.*, vol. 30, no. 1, pp. 116–125, Jan. 1994.

[7] P. Huang, G. Liao, Z. Yang, J.-T. Ma, J. Ma, and X.-G. Xia, "Long-time coherent integration for weak maneuvering target detection and high-order motion parameter estimation based on keystone transform," *IEEE Trans. Signal Process.*, vol. 64, no. 15, pp. 4013–4026, Aug. 2016.

[8] Z. Sun, X. Li, W. Yi, G. Cui, and L. Kong, "Detection of weak maneuvering target based on keystone transform and matched filtering process," *Signal Process.*, vol. 140, pp. 127–138, Nov. 2017.

[9] X. Rao, H. H. Tao, J. Su, X. L. Guo, and J. Z. Zhang, "Axis rotation MTD algorithm for weak target detection," *Digit. Signal Process.*, vol. 26, pp. 81–86, Mar. 2014.

[10] J. Xu, J. Yu, Y.-N. Peng, and X.-G. Xia, "Radon-Fourier transform for radar target detection, I: Generalized Doppler filter bank," *IEEE Trans. Aerosp. Electron. Syst.*, vol. 47, no. 2, pp. 1186–1202, Apr. 2011.

[11] X. Chen, J. Guan, N. Liu, and Y. He, "Maneuvering target detection via radon-fractional Fourier transform-based long-time coherent integration," *IEEE Trans. Signal Process.*, vol. 62, no. 4, pp. 939–953, Feb. 2014.

[12] X. Li, G. Cui, W. Yi, and L. Kong, "Coherent integration for maneuvering target detection based on radon-Lv's distribution," *IEEE Signal Process. Lett.*, vol. 22, no. 9, pp. 1467–1471, Sep. 2015.

[13] B. Boashash and P. O'Shea, "Polynomial Wigner-Ville distributions and their relationship to time-varying higher order spectra," *IEEE Trans. Signal Process.*, vol. 42, no. 1, pp. 216–220, Jan. 1994.

[14] P. Suresh, T. Thayaparan, T. Obulesu, and K. Venkataramaniah, "Extracting micro-Doppler radar signatures from rotating targets using Fourier–bessel transform and time–frequency analysis," *IEEE Trans. Geosci. Remote Sens.*, vol. 52, no. 6, pp. 3204–3210, Jun. 2014.

[15] F. Hlawatsch and G. F. Boudreaux-Bartels, "Linear and quadratic time-frequency signal representations," *IEEE Signal Process. Mag.*, vol. 9, no. 2, pp. 21–67, Apr. 1992.

[16] K. Saho, T. Sakamoto, T. Sato, K. Inoue, and T. Fukuda, "High-resolution UWB Doppler radar interferometric imaging algorithm for multiple moving targets with smoothed pseudo Wigner distribution," *Tech. Rep. IEICE*, vol. 110, no. 250, pp. 261–266, Oct. 2010.

[17] T. Sakamoto, T. Sato, P. J. Aubry, and A. G. Yarovoy, "Texture-based automatic separation of echoes from distributed moving targets in UWB radar signals," *IEEE Trans. Geosci. Remote Sens.*, vol. 53, no. 1, pp. 352–361, Jan. 2015.

[18] M. Setsu and S. Kidera, "Super-resolution Doppler velocity estimation by Gaussian-kernel based range-Doppler conversion for UWB radar," in *Proc. Prog. Electromagn. Res. Symp. (PIERS)*, Nov. 2017, pp. 1306–1311.

[19] S. Kidera, T. Sakamoto, and T. Sato, "Accurate UWB radar three-dimensional imaging algorithm for a complex boundary without range point connections," *IEEE Trans. Geosci. Remote Sens.*, vol. 48, no. 4, pp. 1993–2004, Apr. 2010.

[20] M. Noto, F. Shang, S. Kidera, and T. Kirimoto, "Super-resolution time of arrival estimation using random resampling in compressed sensing," *IEICE Trans. Commun.*, vol. E101.B, no. 6 pp. 1513–1520, Jul. 2018.

[21] Y. Abe, S. Kidera, and T. Kirimoto, "Accurate and omnidirectional UWB radar imaging algorithm with RPM method extended to curvilinear scanning model," *IEEE Geosci. Remote Sens. Lett.*, vol. 9, no. 1, pp. 144–148, Jan. 2012.

[22] A. Yamaryo, T. Takatori, S. Kidera, and T. Kirimoto, "Range-point migration-based image expansion method exploiting fully polarimetric data for UWB short-range radar," *IEEE Trans. Geosci. Remote Sens.*, vol. 56, no. 4, pp. 2170–2182, Apr. 2018.

[23] R. Aiello and A. Batra, *Ultra Wideband Systems: Technologies and Applications*. Boston, MA, USA: Newnes, 2006, pp. 17–52.

[24] S. Kidera, T. Sakamoto, and T. Sato, "Super-resolution UWB radar imaging algorithm based on extended capon with reference signal optimization," *IEEE Trans. Antennas Propag.*, vol. 59, no. 5, pp. 1606–1615, May 2011.

[25] S. Kidera, T. Sakamoto, and T. Sato, "High-resolution 3-D imaging algorithm with an envelope of modified spheres for UWB through-the-wall radars," *IEEE Trans. Antennas Propag.*, vol. 57, no. 11, pp. 3520–3529, Nov. 2009.

[26] V. U. Zavorotny and A. G. Voronovich, "Comparison of geometric optics and diffraction effects in radar scattering from steep and breaking waves," in *Proc. IEEE Int. Geosci. Remote Sens. Symp. (IGARSS)*, Jul. 2007, pp. 1350–1353.

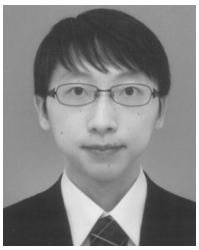

Masafumi Setsu received the B.E. degree in electrical and electronic engineering from the Kisarazu National College of Technology, Chiba, Japan, in 2016, and the M.E. degree in informatics and communication engineering from the University of Electro-Communications, Tokyo, Japan, in 2018.

He joined Anritsu Corporation, Atsugi, Japan, in 2018.

Takumi Hayashi received the B.E. degree in communication engineering and informatics from the University of Electro-Communications, Tokyo, Japan, in 2018, where he is currently pursuing the M.E. degree with the Graduate School of Informatics and Engineering.

His research interest includes advanced radar signal processing for ultrawideband radar systems.

Jianghaomiao He received the B.E. degree in electrical and electronic engineering from the Baoji University of Arts and Sciences, Baoji, China, in 2017. He is currently pursuing the M.E. degree with the Graduate School of Informatics and Engineering, University of Electro-Communications, Tokyo, Japan.

His research interests include signal processing for microwave radar as well as its applications.

Shouhei Kidera (S'05–A'09–M'11) received the B.E. degree in electrical and electronic engineering and the M.E. and Ph.D. degrees in informatics from Kyoto University, Kyoto, Japan, in 2003, 2005, and 2007, respectively.

He has been with the Graduate School of Informatics and Engineering, University of Electro-Communications, Tokyo, Japan, since 2009, where he is currently an Associate Professor. He was a Visiting Researcher with the Cross-Disciplinary Electromagnetics Laboratory, University of Wisconsin Madison, Madison, WI, USA, in 2016. He has been a Principal Investigator of the PRESTO Program of the Japan Science and Technology Agency (JST), Saitama, Japan, from 2017 to 2021. His research interests include advanced radar signal processing or electromagnetic inverse scattering issue for ultrawideband (UWB) 3-D sensor or biomedical applications.

Dr. Kidera is a member of the Institute of Electronics, Information, and Communication Engineers of Japan (IEICE), the Institute of Electrical Engineering of Japan (IEEJ), and the Japan Society of Applied Physics (JSAP). He was a recipient of the 2012 Ando Incentive Prize for the Study of Electronics, the 2013 Young Scientist's Prize by the Japanese Minister of Education, Culture, Sports, Science and Technology (MEXT), and the 2014 Funai Achievement Award.